

The Different Distribution of Gaussian Components between Mainpulse and Interpulse in Pulsar Radio Profiles

HAN Xiao-hong¹ YUEN Rai^{1,2,3†}

(1 *Xinjiang Astronomical Observatory, Chinese Academy of Sciences, Urumqi 830011*)
(2 *Key Laboratory of Radio Astronomy, Chinese Academy of Sciences, Nanjing 210023*)
(3 *School of Physics, University of Sydney, Sydney NSW 2006*)

ABSTRACT The arrangement of Gaussian emission components along a trajectory traced by a visible point moving at non-uniform speed as the pulsar rotates is investigated. By assuming emission locations confined to spots that arranged evenly around the magnetic axis, a Gaussian emission component corresponds to a cut of an emission spot by the trajectory. The distribution of the emission spots, and hence the Gaussian components, are uneven along the trajectory, being highest around the nearest approach of the magnetic axis to the line of sight, and dependent on two angles of a pulsar: the viewing angle, between the rotation axis and the line of sight, and the obliquity angle, between the magnetic and rotation axes. Observed multiple Gaussian components in a profile then corresponds to several emission spots locating on the trajectory within a specific range of pulsar phase. Demonstration is given to show that the number and distribution of the Gaussian components are different between ranges around the near and far sides of pulsar rotation, corresponding to the mainpulse and interpulse, respectively. The total number of emission spots on a trajectory may be different from that around the magnetic axis, and ignoring the motion of the visible point can lead to significant discrepancy in the predicted number of emission spots. The shape and number of the Gaussian components for fitting a profile may be different from that of the actual components that compose the profile. As an example, the model is applied to the emission arrangement in PSR B0826–34 by assuming the emission comes from a single pole.

Key words radiation mechanisms: non-thermal, pulsars: general, methods: analytical

Classified index: P145; **Document code:** A

Received 2021-07-02, revised version 2021-10-27

*Supported by the Natural Science Foundation of China (NSFC) (Grant Nos. U1838109, 11873080, 12041301); the Open Program of the Key Laboratory of Xinjiang Uygur Autonomous Region (Grant No. 2020D04049); and the 2018 Project of Xinjiang Uygur Autonomous Region of China for Flexibly Fetching in Upscale Talents

†ryuen@xao.ac.cn

1 Introduction

Investigation of pulsar average radio profiles reveals that they come with vastly different shapes implying that each possesses unique emission arrangement whose details can be obtained by studying the profile characteristics^[1–5]. An important approach for the latter is to consider each individual profile as a superposition of several emission components of Gaussian shape^[6–8]. By using a fitting procedure for the set of parameters that minimizes the residuals between the observed profile and the Gaussian components, important details on the geometric arrangements of the emitting structures and the related radio radiation mechanism in the pulsar can be analyzed^[1–3, 8–14]. In principle, the technique is applicable to pulsar profiles of any complexity. Applying to interpulses, second identifiable emission appears roughly at half of a pulsar rotation, the method shows that the number and shape of the fitting emission components are sometimes different from that of the mainpulses. The goal of this paper is to examine the arrangement of Gaussian components at different pulsar phases, and how they relate to the viewing geometry of a pulsar, in particular the viewing angle, ζ , between the rotation axis and the line of sight, and the obliquity angle, α , between the magnetic and the rotation axes.

Arrangement of the Gaussian emission components in a profile usually involves making assumptions for the viewing geometry of the pulsar and the underlying emitting patterns, such as in terms of emission from discrete regions^[1–3, 12–13]. A widely accepted emission model assumes that the emission regions are confined into several isolated and discrete circular sub-beams located on a carousel rotating around the magnetic axis^[15–22]. In this carousel model, the sub-beams flow around the magnetic axis relative to the surface of the

star through the line of sight. A description for the distribution of sub-beams in azimuthal direction around the magnetic axis is attributed to a standing wave at a specific spherical harmonic. The standing wave is determined by an instability in the magnetosphere resulting in a periodic pattern of overdense (sub-beams) and underdense regions of plasma, forming a structure that varies $\propto \cos(m\phi_b)$ ^[23–24], where m is the emission region number in integer and ϕ_b is the azimuthal angle around the magnetic axis. A favoured instability is the diocotron instability^[25–26], although alternatives have also been proposed^[23–24]. While the distribution of individual m as functions of height, r , and polar angle, θ_b , is unclear, we assume that radio emission in this version of carousel model appears to come from discrete regions, corresponding to m regions arranged evenly in azimuth around the magnetic axis. Visibility of emission from the regions can then be established by assuming that visible emission from a source point is directed along the local magnetic field line of dipolar structure and parallel to the line of sight. The source point is located within the polar cap region that is bounded by the last closed field lines. Two angles define the geometry, namely ζ and α . An explicit solution for the geometry gives the angular position of the “visible point” as a function of the pulsar phase, ψ . As the pulsar rotates, the visible point moves at non-uniform angular speed ω_V , and traces out a closed path after one pulsar rotation, from where emission is visible to an observer^[27]. We refer to an emission region from which emission is visible to an observer as an emission spot. The traditional assumption of a stationary visible point is valid strictly for $\alpha = 0$.

In this paper, we investigate the distribution of the Gaussian emission components at different pulsar phases, and its relationship with ζ and α based on a purely geometric model. We discuss

the viewing geometry and the emission structure used for this investigation in Section 2. In Section 3, we demonstrate the differences in the number of emission spots for a fixed range of rotational phase along different parts of a trajectory traced by the visible point for different ζ , α , and compare them to the scenario where ω_V is ignored. We consider the emission arrangement in PSR B0826–34 incorporating the motion of the visible point as an example. We discuss our results and conclude the paper in Section 4.

2 Regions of visible emission

In this section, we summarize the viewing geometry and emission structure for observable emission.

2.1 Geometry for visible pulsar emission

We assume Cartesian coordinates in which the observer and magnetic frames are represented by $\hat{x}, \hat{y}, \hat{z}$ and $\hat{x}_b, \hat{y}_b, \hat{z}_b$, with $\hat{z} = \hat{\omega}_*$ and $\hat{z}_b = \hat{M}$ along the rotation and magnetic axes of a pulsar, respectively, where ω_* is the spin frequency of the star and the subscript b represents quantities in the magnetic frame. The respective unit vectors in spherical coordinates $\hat{r}, \hat{\theta}, \hat{\phi}$ and $\hat{r}_b, \hat{\theta}_b, \hat{\phi}_b$ are related by the transformation matrices given in the Appendix 4. In the magnetic frame, the equation for a dipolar field line originating from an azimuthal position, ϕ_b , on the star's surface is defined by $r = r_0 \sin^2 \theta_b$ where r_0 is the field line constant.

We describe pulsar visibility based on an idealized model in which radiation originates from the source point that locates only within the open-field region^[28–29], and the radiation is directed tangentially to the local dipolar magnetic field line^[30] and parallel to the line-of-sight direction^[27]. Designating the polar coordinates of a visible emission in the observer's and magnetic frames by (θ_V, ϕ_V)

and (θ_{bV}, ϕ_{bV}) , respectively, a visible point can be defined in the observer's frame by $\theta = \theta_V(\zeta, \alpha; \psi)$ and $\phi = \phi_V(\zeta, \alpha; \psi)$ or by (θ_{bV}, ϕ_{bV}) in spherical polar coordinates. The visible point in the magnetic frame is given by^[27, 31]

$$\begin{cases} \cos 2\theta_{bV} &= \frac{1}{3} (\cos \theta_c \sqrt{8 + \cos^2 \theta_c} - \sin^2 \theta_c) , \\ \tan \phi_{bV} &= \frac{\sin \zeta \sin \psi}{\sin \alpha \cos \zeta - \cos \alpha \sin \zeta \cos \psi} , \end{cases} \quad (1)$$

where $\cos \theta_c = \cos \alpha \cos \zeta + \sin \alpha \sin \zeta \cos \psi$, and ψ is measured from the plane where θ_c is minimum, or $\theta_c = \beta = \zeta - \alpha$, with β being the impact parameter. For given ζ and α , the visible point traces out a closed path on a sphere of radius, r , in the magnetosphere after one pulsar rotation, which we refer to as the trajectory of the visible point. The geometry identifies the center of the pulse profile at the near side to the observer at $\psi = 0$ where the rotation axis, magnetic axis and the line of sight are coplanar, and $\theta_c = \beta$. We also choose the zeros of all the three azimuthal angles to coincide at $\phi_b = \phi = \psi = 0$. Assuming that emission comes only from open-field regions restricts the radiation source be located at heights greater than a height, r_V , given by^[27]

$$r_V = \frac{r_L \sin^2 \theta_{bV}}{\sin^2 \theta_{bL}(\phi_{bV}) \sin \theta_L(\phi_{bV})} , \quad (2)$$

where θ_{bL} is the polar angle of the point on the last closed field line at ϕ_{bV} , and θ_L is the angle measured from the rotation axis to the point where the last closed field line is tangent to the light cylinder. Here, $r_L = c/\omega_*$ is the light-cylinder radius and c is the light speed. The minimum and maximum of r_V occur at $\psi = 0$ and 180° , respectively, in our model. The derivation of Equation (2) is based on the last closed field lines, which are determined by the condition that the field lines are tangent to the light cylinder, and the trajectory of the visible point is tangent to the locus of the last closed

field lines^[27]. Therefore, Equation (2) defines the minimum heights along the trajectory from which emission is detectable. Emission occurring on the last closed field line is visible only from $r = r_V$. Open field lines satisfy $r_0 > r_L$, and emission is visible from such field lines only for $r > r_V$. It implies that the minimum height for visible emission from an open-field region is $r = r_V$, which is on the boundary of the region (cf. Section 2.3). The height of a point from which emission is visible is larger than r_V for field lines located closer to the magnetic axis.

An oblique rotator results in variations in the instantaneous angular velocity of the visible point, ω_V , along the trajectory of the visible point given by^[27]

$$\omega_{V\theta} = \omega_* \frac{\partial\theta(\alpha, \psi)}{\partial\psi}, \quad \omega_{V\phi} = \omega_* \frac{\partial\phi(\alpha, \psi)}{\partial\psi}, \quad (3)$$

where $\omega_* = d\psi/dt$, and $\omega_{V\theta}$ and $\omega_{V\phi}$ are two components along the polar and azimuthal directions, respectively. The visible point sub-rotates and reaches the lowest speed when the magnetic axis is on the near side of the pulsar around $\psi = 0$, but large for a small range around $\psi = 180^\circ$, where the emission point super-rotates and reaches the maximum speed when the magnetic axis is on the far side of the pulsar at $\psi = 180^\circ$. The average angular speed over one pulsar rotation is $\langle\omega_V(\psi)\rangle = \omega_*$.

2.2 The emission structure

The complicated shape of an average profile in radio pulsars is interpreted as being composed of multiple Gaussian components emitting from discrete locations^[6-7]. A purely magnetospheric interpretation for the discrete emission locations involves a standing wave structure at a specific spherical harmonic resulting in a distribution that varies $\propto \cos(m\phi_b)$ around the magnetic axis^[23-24]. A periodic pattern of m enhanced emission regions is formed evenly in azimuth around

the magnetic axis, and radio emission from such arrangement appears to come from discrete regions. The configuration of the m regions in θ_b and r is uncertain. Here we assume that the m regions are arranged in pattern independent of polar angle so that each forms a radial spoke when projected onto a surface of constant r . Furthermore, these spokes are assumed locally independent of height, r . A visible enhanced emission region corresponds to the trajectory of the visible point crossing a spoke, which we refer to as an emission spot.

2.3 Range of visible emission

The visibility of emission requires that (i) an emission point inside an emission spot and both must lie on the trajectory of the visible point, and (ii) the trajectory must lie partly (or entirely) inside an open-field region. The latter introduces a dependence on r for each open-field line with $r = r_V$ corresponding to the emission point on the last closed field line. The open-field region has a boundary that is fixed relative to the magnetic axis, so that it rotates with the star. The size of the region enclosed by this boundary increases with r , such that it defines the polar cap at the stellar surface, where $r = r_*$, and it extends to all angles for $r \gtrsim r_L$. The pulse-width may be interpreted in terms of the range of ψ on the trajectory that lies inside an open-field region and bounded by the points of intersection between the trajectory and the boundary of the open-field region, with the specific value of the fiducial point, ψ_0 , dependent on the pulsar model. Within the pulse-width, the visible point moves along the trajectory with length that is dependent on $r - r_V > 0$, with the pulse-width proportional to $r - r_V$.

Fig. 1 shows the trajectory of the visible point (solid black) for $\zeta = 10^\circ$ and $\alpha = 20^\circ$, together with three open-field regions with boundaries denoting equal height at $1.4 \times 10^{-2}r_L$ (dotted gray),

$7 \times 10^{-2}r_L$ (dot-dashed gray) and $0.14r_L$ (solid gray). The coordinates of a point (x_b, y_b) in the plot is the Cartesian representation for the coordinate pair (θ_b, ϕ_b) , and hence the magnetic axis is located at the origin. The relations between the two coordinates are such that a line connecting the origin to the point has length defined by θ_b , and the angle between the positive x_b -axis and the line has range given by ϕ_b . Note that the trajectory does not enclose the magnetic axis. Here, we consider two scenarios. In scenario (i), the motion of the visible point is nonzero, which indicates that the location of visible emission is given by Equation (1). As discussed in Section 2.1, ω_V varies as a function of ψ , where $\omega_V < \omega_*$ around $\psi = 0$, and the visible point moves in the direction of pulsar rotation^[27]. Scenario (ii) ignores the motion of the visible point. This corresponds to visible emission originating from a point where emission is parallel to the line (the line of sight in this case) that passes through the center of the star. As the pulsar rotates, the line remains fixed such that the visible point is stationary in the observer's frame and the open-field region moves across the visible point at a constant rate at ω_* . Consider first the scenario (i), which is represented by the trajectory in solid black. Emission is visible from height r only when the trajectory lies within the boundary of an open-field region, and the edges of the pulse window are defined by ψ when the trajectory cuts the boundary. A more restrictive assumption relates to emission occurring only on the last closed field line, and the emission can be seen from only one point of height $r = r_V$. This is indicated by the inner open-field region, bounded by the curve in dotted gray, with which the trajectory touches its boundary at one point where emission is detectable from that point only. For the open-field region bounded by the curve in dot-dashed gray, the trajectory

cuts it from points A to B between which the trajectory lies inside. Their longitudinal phases are $\psi_A = -90^\circ$ and $\psi_B = 90^\circ$ giving the range of observable emission $\Delta\psi = \psi_B - \psi_A = 180^\circ$. A special case is shown with the outer open-field region, bounded by the curve in solid gray, where the trajectory is enclosed entirely in the region. This implies that emission from locations that coincide with any points on the trajectory is observable giving a pulse-width that spans over the entire pulsar rotation. For scenario (ii), the location of the visible point is fixed at a polar angle $\theta = \theta_V$ at $\psi = 0$ in the observer's frame and the open-field region moves across it as the pulsar rotates. Transforming to the magnetic frame using the equations in the Appendix4 gives a path that is different from the trajectory of the visible point, as shown by the dotted black curve. The discrepancies are due to omission of the changing location of the visible point associated with the variation of ω_V as the pulsar rotates. Here, the path intersects the inner region at the same point as the trajectory of the visible point. For the open-field region in the middle, it intersects the boundary differently at locations A' and B' where $\psi_{A'} = -50^\circ$ and $\psi_{B'} = 50^\circ$ giving a pulse-width that is almost 45% narrower. The different path means that emission originates from different set of open-field lines with $r_0 > r_L$, and $r = 1.4 \times 10^{-2}r_0$ at $\psi = 0$. Instead of enclosed by the outer region, as with the trajectory of the visible point, the path intersects the region at points C and D , with $\psi_C = -75^\circ$ and $\psi_D = 75^\circ$. This implies that emission is observable only at locations where the path lies inside the region and between ψ_C and ψ_D . The required height at the boundary of an open-field region to enclose the entire path is now $0.32r_L$, which is higher by more than twice of the value when the motion of the visible point is included.

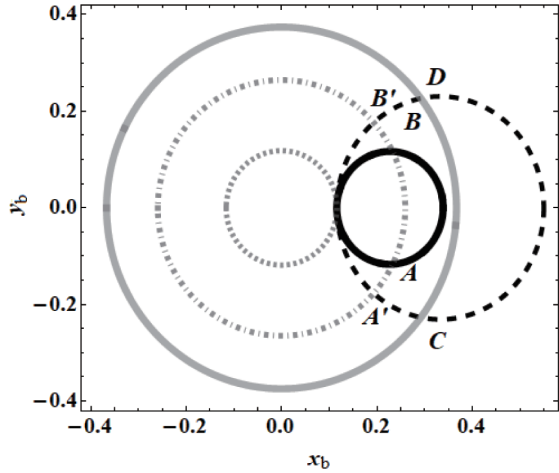


Fig. 1 Simulations for different pulse-widths based on three open-field regions with boundaries at increasing height from inner at $1.4 \times 10^{-2} r_L$ (dotted gray) to outer at $0.14 r_L$ (solid gray) for a trajectory of the visible point (solid black) using $\zeta = 10^\circ$ and $\alpha = 20^\circ$. The magnetic pole is located at the origin. See text for explanation of the points A , B , A' , B' , C and D . Also shown is another path (dotted black) for visible emission where the motion of the visible point is ignored. Note that x_b and y_b are normalized.

3 Distribution of emission spots

In this section, we show that the distribution of emission spots, corresponding to the distribution of the Gaussian components, along the trajectory of the visible point is uneven and generally different from that around the magnetic axis. We also examine the significance of ignoring ω_V .

3.1 Along the trajectory of the visible point

We simulate four trajectories of the visible point in the ψ - ϕ_b plane that is constructed similar to the equirectangular projection for mapping a globe. In this representation, the distances along the line of longitudes are conserved such that the magnetic pole is a vertical line along $\psi = 0$ as

shown in Fig. 2, which shows the variations of ϕ_{bV} along the trajectory of the visible point as a function of ψ for different values of $\{\zeta, \alpha\}$. For better illustration, 20 radial spokes (gray horizontal bands) are assumed evenly in azimuth around the magnetic axis giving horizontal rows of spoke with the two spokes centered at $\phi_b = -180^\circ$ and $\phi_b = 180^\circ$ coinciding with each other. Pulsar rotation is counterclockwise when looking directly down the rotation axis where the direction of rotation is pointing upward. As the pulsar rotates, the visible point moves starting from $\psi = -180^\circ$ and advances to more positive ψ tracing out a trajectory that ends at $\psi = 180^\circ$ after one complete pulsar rotation. According to Equation (1), a corresponding traversal in ϕ_b that covers from -180° to 180° signifies a complete revolution around the magnetic axis. The evolution of ϕ_b is different for different trajectories as shown in Fig. 2. For a trajectory with $\beta > 0$, such as the one in solid blue, the variation in ϕ_b first decreases negatively towards and approaches -180° as ψ increases, and reaches $\phi_b = 180^\circ$ at $\psi = 0$, where the visible point is located between the magnetic axis and the equator. It then decreases as ψ increases and returns to $\phi_b = 0$ forming a complete rotation around the magnetic axis. For a trajectory with $\beta < 0$, as the one in solid black, the variation of ϕ_b is also increasing negatively to a minimum ($> -180^\circ$), then decreases and reaches $\phi_b = 0$ at $\psi = 0$, where the visible point is located between the magnetic and rotation axes. It then increases again positively reaching a maximum ($< 180^\circ$), then decreases and returns to $\phi_b = 0$. Variation in ϕ_{bV} along a trajectory as the pulsar rotates results in cutting spokes in the process with the number that is dependent on ζ, α . Fig. 2 shows that not all trajectories enclose the magnetic axis. A complete revolution around the magnetic axis occurs only for the trajectories in blue and brown, both with positive β , whereas a

partial coverage is seen for trajectories in black and green, whose β values are negative.

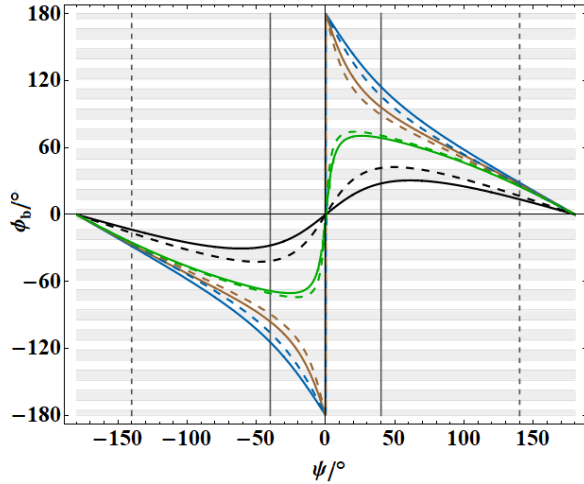


Fig. 2 Variations of ϕ_b along the trajectory of the visible point as a function of ψ for $\{\zeta, \alpha\} = \{30^\circ, 15^\circ\}$ (solid blue), $\{10^\circ, 20^\circ\}$ (solid black), $\{40^\circ, 30^\circ\}$ (solid brown) and $\{40^\circ, 43^\circ\}$ (solid green). A stationary 20-spoke structure is shown for $-180^\circ \leq \phi_b \leq 180^\circ$ with each spoke assumed of 9° in width. Radial spokes at the same ϕ_b line up and appear as a single spoke (gray horizontal band) in the ψ - ϕ_b plane. Evolution of a trajectory is toward more positive ψ . Trajectories are not straight lines indicating non-uniform variation of ϕ_{bV} resulting in uneven distribution of emission spots on a trajectory. Also shown are two pulse windows, each of width 80° , centered at $\psi = 0$ and bounded by two gray vertical lines, and at $\psi = 180^\circ$, bounded by two vertical dashed lines, within which each trajectory intersects different number of spokes. The dotted curves represent paths that traced by a visible point using the same ζ, α of the corresponding color but with ω_V omitted.

A uniform distribution of radial spokes around the magnetic axis does not imply evenly distributed emission spots along the trajectory of the visible point. For nonzero ζ, α , variation of ϕ_{bV} along a trajectory is large for ranges around $\psi = 0$ then reduces toward $\psi = \pm 180^\circ$. A special case relates

to $\zeta = 0$ (not shown) where ϕ_{bV} is a constant resulting in a horizontal line. A larger change in ϕ_{bV} for a given change in ψ means that more emission spots are visible as the trajectory cuts more spokes. Considering $-40^\circ \leq \psi \leq 40^\circ$ (between two vertical solid gray lines) in Fig. 2, the corresponding coverage of $\Delta\phi_b = \Delta\phi_{bV}$ is 131° (solid blue), 56° (solid black), 168° (solid brown) and 137° (solid green) cutting 7, 3, 9 and 7 entire spokes, respectively, where the last trajectory also cuts a fraction of two spokes centered at $\phi_b = \pm 72^\circ$. However, the corresponding changes in ϕ_b for the same amount of changes in ψ at around $\psi = \pm 180^\circ$ are smaller.

A different view on the uneven number of observable emission spots for a given range of ψ along a trajectory of the visible point is through the consideration of the change of ϕ_{bV} in terms of ψ . Fig. 3 shows the variation in $\Delta\phi_{bV}/\Delta\psi$ as a function of ψ for the same ζ and α combinations used in Fig. 2. A negative value indicates that a trajectory is advancing in the opposite ϕ_b direction, as seen by the case with the trajectories in black and green for $|\psi| \gtrsim 50^\circ$. A special case is shown for $\zeta = 0$ (red) where the ϕ_{bV} is a constant resulting in a horizontal line at $\Delta\phi_{bV}/\Delta\psi = 0$. In general, $\zeta \neq 0$ and the curves peak at around $\psi = 0$, with the change in $\Delta\phi_{bV}/\Delta\psi$ becoming steeper as β lowers for a given α . Cutting of a radial spoke by the trajectory is signified by the traversal of the latter through all or part of the spoke in ϕ_b , and more spokes are cut for a broader coverage in ϕ_b . Therefore, $\Delta\phi_V/\Delta\psi$ may be treated as the density of spokes cutting by a trajectory of given ζ, α . The density increases as ψ approaches zero (more spokes are cut) and decreases as $|\psi|$ increases. Variations in the density then imply uneven distribution of emission spots, corresponding to different numbers of Gaussian components, along the trajectory with the emission spots appearing to bunch up more around $\psi = 0$ where the density is highest.

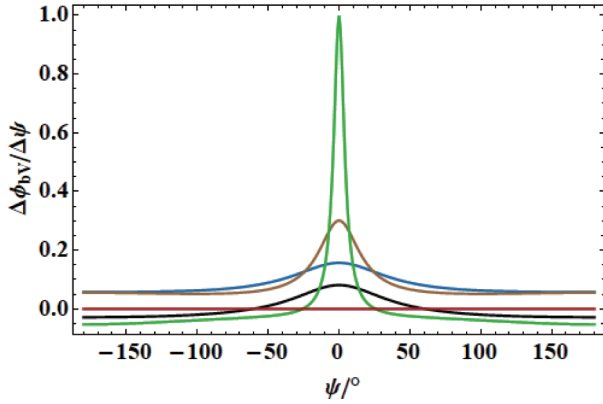


Fig. 3 Normalized $\Delta\phi_{bv}/\Delta\psi$ as a function of ψ indicating changes in the density of observable emission spots as a function of ψ along the trajectory of the visible point for the same four combinations of ζ, α in Fig. 2. The red horizontal line indicates $\zeta = 0, \alpha = 60^\circ$. Note that absolute values are taken for the blue and brown curves.

3.2 Distribution around the far side of rotation

Figs. 2 and 3 suggest that an unequal amount of emission spots is cut at near $\psi = 180^\circ$ as compared to that around $\psi = 0$. The number of radial spokes cut by each trajectory for the same $\Delta\psi$ (between the two vertical dotted lines) centered at $\psi = 180^\circ$ is 3 (solid blue), 1 (solid black), 3 (solid brown) and 3 (solid green) as shown in Fig. 2, which is less than that cut at around $\psi = 0$ as each covers a smaller range of ϕ_b . For emission coming from a single magnetic pole and a profile with the fiducial point located at $\psi = 0$, the number of constituting emission components for a profile centered at $\psi = 0$ is different from that at $\psi = 180^\circ$ for identical $\Delta\psi$, with the former being larger. It follows that, if each emission spot radiates equally, the flux density of a profile is weaker around $\psi = 180^\circ$ as it comprises lesser emission spots, corresponding to fewer Gaussian components.

3.3 Total observable emission spots

An emission is detectable only if the corresponding emission spot lies on the trajectory of the visible point. It follows that the estimation of the total number of emission spots is along the trajectory of the visible point, which may or may not enclose the magnetic axis. This yields a number that may be different from that located around the magnetic axis. A prominent example is that shown with the trajectory in black in Fig. 2 where the observed number of emission spots are different from the assumed $m = 20$. For the cases considered in Fig. 2, only the trajectories in solid blue and solid brown, both with positive β , give a prediction of 20 emission spots, whereas the others give a lower values at 6 (solid black) and 16 (solid green).

3.4 Omission of ω_V

The significance of the motion of the visible point is revealed by considering another scenario in which the visible point is assumed stationary, as discussed in Section 2.3. The resulting path traced by the visible point for each of the combinations of ζ, α in Fig. 2 is shown in dotted lines of the corresponding color. The two scenarios coincide at only two points at $\psi = 0$ and 180° , and the greatest discrepancies occur around $\psi = 0$ where the line of sight is closest to the magnetic axis in the model. The range of ϕ_b covered by each path is also different with $\Delta\phi_b = 148^\circ$ (dotted blue), 83° (dotted black), 181° (dotted brown) and 142° (dotted green) for $|\psi| \leq 40^\circ$. The number of predicted emission components for the corresponding path are 9, 5, 11 and 9 for $|\psi| \leq 40^\circ$ and 3 for all trajectories for $|\psi| \geq 140^\circ$. While the total number of predicted emission spots for the trajectories in blue, brown and green remains the same, it is different for the trajectory in black with a total of 10 emission spots predicted. The deviations are expected to be more significant when the constraints

on the height of an open-field region is imposed as shown in Fig. 1. This is because the path that traverses an open-field region of a particular height is longer when ω_V is omitted implying that more emission spots are cut. However, $\Delta\psi$ actually diminishes meaning that the visible point spends a shorter time in an open-field region.

3.5 Profile with small $\Delta\psi$ and β

The assumption that pulsar radio profiles can be represented by multiple components of Gaussian shape^[7-8, 32] represents an essential technique for studying pulsar emission structures and properties. The identification of the constituting components of a profile is achieved by fitting a sum of Gaussian components to the profile of interest. To avoid over-fitting, a measure of some kind is established for comparison of the fitted and observed profiles and one will stop adding components to the fitting once the value given by the measure is below a certain threshold^[6]. As the amount of fitting components is different for different pulsars^[6], an important aspect of such analysis relates to the questions of the “true” number of the “real” components. This is due to the fact that the obliquity angles of many pulsars are unknown and hence it lacks a method to estimate the true number of the constituting Gaussian components. Failure of such decomposition is a known effect if the observed profile is not well resolved resulting in the fitting being not unique or even correct. This introduces bias in subsequent analysis for the emission properties of the pulsar.

In general, the number of emission spots cut by a trajectory of the visible point is dependent on the viewing geometry such that the former increases as $|\beta|$ decreases for a fixed $\Delta\psi$. It is consider a scenario where $\alpha = 30^\circ$ and $\beta = 0.5^\circ$, which gives nine emission spots for $\Delta\psi = 10^\circ$. Next, we

construct the Gaussian component for each of the emission spot by randomly¹ generating the amplitude, J , between 0.1 and 1, pulse-width, σ , based on one-fifth to full size of a radial spoke in degrees, and the position of peak phase, ψ_p , that fits within $\Delta\psi = 10^\circ$. The organization of the components is such that σ decreases as the peak phase ($|\psi_p|$) increases toward the two boundaries of the profile. The profile is then given by the sum of all the components with the intensity varies as^[6-7, 11]

$$I(\psi) = \sum_{i=1}^N J_i \exp \left[-\frac{(\psi - \psi_{p,i})^2}{2\sigma_i^2} \right], \quad (4)$$

where I is the intensity of the profile as a function of ψ , i signifies the i th Gaussian component, and N is the total number of components, which is nine in this case. Table 1 lists the parameters required for simulating and fitting the same profile. The parameters for each Gaussian component are given in the upper panel of Table 1, and their shapes and the resulting profile are shown in Fig. 4. Note that random noise has been added to the resulting profile to mimic real observation. The simulated profile in Fig. 4 would represent an observed profile. Assuming no knowledge of the original components, we try to fit the same profile (with noise) using different sets of Gaussians, each containing different number of components from one to eight. Then, the observed profile is simulated for 100 times, each with different random noise, and an average value for the residual sum of squares (RSS) from the fitting is calculated for each set. Fig. 5 shows the fitting for the original profile shown in Fig. 4. The least number of Gaussian components that gives the best fitted profile is shown in gray and red, respectively, in Fig. 5, with the latter overlaying with the original profile (black). The parameters are given in the lower panel of Table 1. From Fig. 5, the residuals for the difference between the fitted

¹We explored different configurations, both random and organized, and obtained similar results.

and simulated profiles exhibit random scattering around zero with the mean and maximum values given by -8×10^{-4} and 0.07 in intensity, respectively. The average RSS is about 5.8. As a comparison, using the original nine Gaussian components (in Fig. 4) for the fitting also gives RSS of about 5.8 in average. This suggests that the fitting using the four Gaussian components is reasonably well. However, it is clear from Fig. 5 that the number of Gaussian components needed to fit the profile, N_F , is different from the actual number of components, N_C , that composes it. In general, we find that $N_F \leq N_C$.

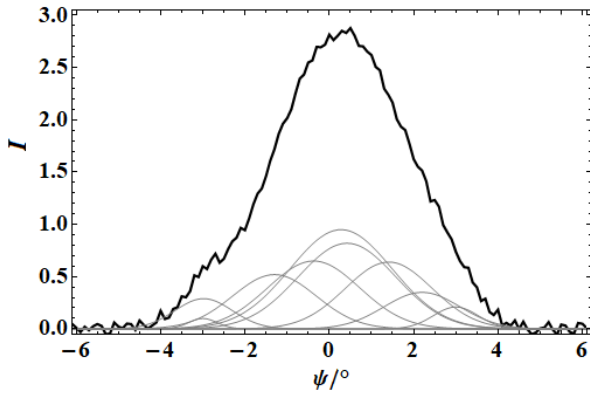


Fig. 4 Simulation of the profile (black) using nine Gaussian components (gray) based on the parameters in Table 1 for $\beta = 0.5^\circ$ and $\alpha = 30^\circ$ within a pulse-width of 10° centered at $\psi = 0$. Random noise has been added to the resulting profile.

3.6 An example case: PSR B0826–34

Emission from this pulsar can be detected from most of the pulsar rotation resulting in a broad profile^[33–34]. Esamdin et al.^[34] divided the profile in strong-emission mode into four distinct regions based on the emission and subpulse properties, with emission mostly detected in regions I and III. The shapes of the profile from these two regions both imply composition of more than one emission component, with region III display-

ing five discernible components and a similar number of components but more bunched up in region I. Furthermore, the range of detectable emission is also different for the two regions with region I being narrower giving a slightly higher density in emission component. Based on the differences in the variations of the subpulse spacings between the first and second half of the profile, the authors were able to estimate an obliquity angle of 0.5° for this pulsar suggesting that both emission comes from a single magnetic pole^[34].

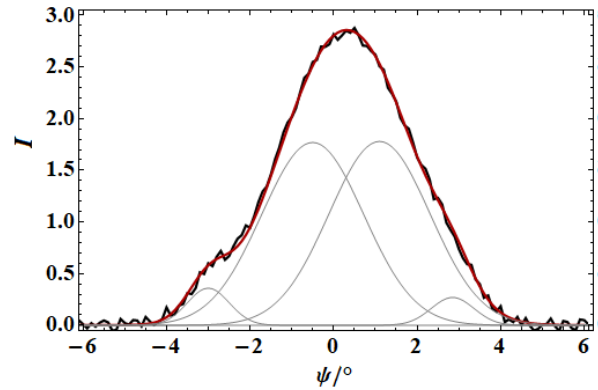


Fig. 5 Fitting for the original profile in Fig. 4 by using fewer Gaussian components (gray). The original and fitted profiles are indicated in black and red, respectively.

We simulate the trajectory of the visible point incorporating the motion of the visible point using the predicted $\alpha = 0.5^\circ$ and an assumed $\beta = 2.3^\circ$. An observed higher density of emission component in region I implies that the corresponding part of the trajectory lies in the range of pulsar phase around $\psi = 0$ in our model. With the reported pulse windows of sizes 94° and 143° for regions I and III^[34], respectively, we divided the trajectory of the visible point into four parts, such that the range between $\psi = \pm 47^\circ$, centered at $\psi = 0$, corresponds to region I and from $\psi = 88.5^\circ$ to -128.5° corresponds to region III. A total number of 14

radial spokes is assumed evenly located around the magnetic axis. Our model predicts an open-field region at height $\gtrsim 13r_*$, where $r_* = 10$ km is the stellar radius, for observable emission to come from the trajectory of the visible point due only to a single magnetic pole. The trajectory revolves around the magnetic axis and traverses ϕ_b from -125° to 125° in total of $\Delta\phi_b = 110^\circ$ for region I, and from 81° to -44° in total of $\Delta\phi_b = 125^\circ$ for region III. A non-uniform spoke density along the trajectory is determined with the highest density occurring in region I and lowest in region III giving an estimation of 5 emission spots in both regions consistent with observation. To simulate the profile with drift phases adjusted, as shown in Fig. 4 by Esamdin et al.^[34], we assume that σ is given by half the spoke size for all Gaussian components, which is $\sigma = 6.4^\circ$ for 14 spokes around the magnetic axis. The peaks for the components as given by our model are located at $\psi = -43.4^\circ, -21.5^\circ, 0, 21.5^\circ, 43.4^\circ$ for region I, and at $\psi = 92.8^\circ, 120.7^\circ, 149.8^\circ, 180^\circ, -149.8^\circ$ for region III. We also assume that the amplitude (J) for the emission spots in region I is twice as that in region III. Fig. 6 shows the profiles in regions I and III coinciding with the reported longitudinal phases. The simulation reproduces several basic features of the observed profile. Firstly, five pulse components are obtained for the two regions, with the separation between components being wider in region III. The pulse-width measured at 10% of the full intensity is also wider in region III than that in region I at 145° and 115° , respectively. In addition, a drop in intensity is seen between any two consecutive pulse components, with the ratio of drop (relative to the average peak intensity of the two immediate adjacent pulse components) being larger in region III, consistent with observation.

The same is seen regardless of J chosen in the two regions. Furthermore, the amount of the intensity drop varies across the simulated profiles. As ψ increases, the amount of drop exhibits decreasing followed by increasing in region I, whereas it is varying in region III. Both are consistent with the observation. Our simulation also indicates variations in the emission spot separation (P_2) across the profile with an average of 22° in region I, consistent with observation, and slightly higher at 29° in region III.

Table 1 Parameters of the Gaussian components for simulation and fitting the same profile are shown in the upper and lower panels, respectively. The numbers are rounded to two decimal places

Component	J	$\psi/^\circ$ (peak)	$\sigma/^\circ$
Simulation			
1	0.10	-3.00	0.34
2	0.29	-2.98	0.68
3	0.52	-1.30	0.99
4	0.65	-0.37	1.09
5	0.95	0.28	1.21
6	0.82	0.42	1.16
7	0.64	1.41	1.03
8	0.35	2.20	0.90
9	0.21	3.00	0.53
Fitting			
1	0.36	-3.00	0.50
2	1.77	-0.50	1.22
3	1.78	1.10	1.21
4	0.27	2.85	0.51

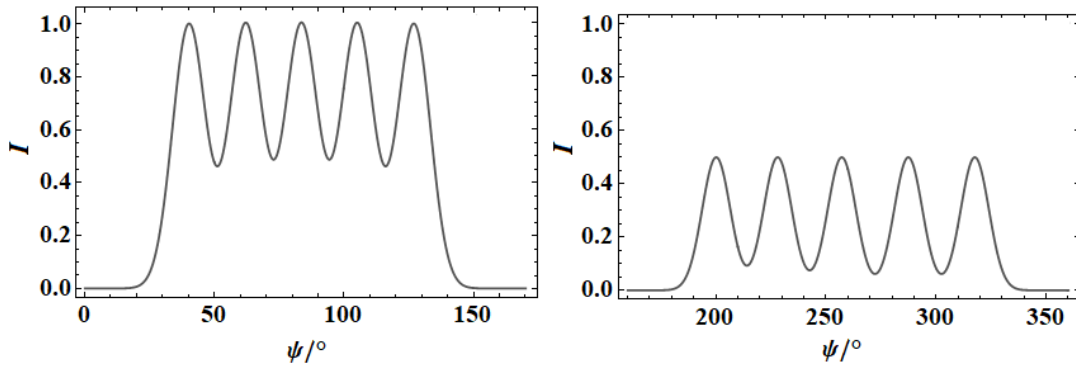


Fig. 6 Simulations for the profile (drift phases adjusted) for regions I (left) and III (right)

4 Discussion and conclusions

We have investigated the distribution of emission components based on a purely geometric model in which detectable emission at a particular ψ comes from a visible point where emission is tangent to the dipolar field line and directed parallel to the line of sight direction. The visible point moves at non-uniform speed as the pulsar rotates tracing out a trajectory that may or may not enclose the magnetic axis. By assuming an emitting structure in which emission is confined to spots that are arranged uniformly around the magnetic axis, a Gaussian emission component corresponds to emission from an emission spot that lies on the trajectory of the visible point. In this model, the distribution of emission spots on the trajectory of the visible point is uneven being highest around $\psi = 0$ and lowest around $\psi = 180^\circ$. We show that the viewing and obliquity angles of a pulsar can affect the amount of emission spots determined along a trajectory, which may be different from the total number of emission spots around the magnetic axis. We compare our model to those with ω_V ignored and find that the predicted number of emission spots can be different both for a given range of $\Delta\psi$ near $\psi = 0$ and along the whole trajectory. We consider PSR B0826–34 as an

example and show that, by treating emission from a single pole and $m = 14$, our model can account for the observed number of emission components, and some related characteristics, in the two emission regions corresponding to the mainpulse and interpulse.

Our model is consistent with the fact that pulsar average radio profiles are generally composed of multiple emission components. This is shown in Fig. 2 where each of the trajectories cuts more than one emission spot regardless of the sign of β . Since the density of emission spots changes as the trajectory traverses longitudinal phases of different $\Delta\phi_{bV}/\Delta\psi$, intersection of multiple emission spots requires that the trajectory is steep around $\psi = 0$ implying small β . This is consistent with most pulsars whose $\beta < 10^\circ$ ^[1] and a typical duty cycle of 0.1 resulting in the trajectory that covers broad $\Delta\phi_{bV}$ and hence cutting multiple emission spots. For pulsars with small β and $\Delta\psi$, the arrangement of the emission spots is such that they locate closely to each other within a narrow range of pulsar phase resulting in overlapping with neighboring Gaussian components. In this case, modest deviations in the emission properties across the emission spots, due to their locations being at different parts of the carousel layer, may be masked by other

components giving an overall simpler profile shape as shown in Fig. 4. This leads to deviation in the prediction of the number of emission spots, which compose the profile, from the number of Gaussian components used for fitting the profile. It also implies that the shape of a profile may appear “simple” but the actual amount of composing emission components may be many.

The prediction of a non-uniform distribution of emission spots along the trajectory of the visible point even for a uniform arrangement of emission spots around the magnetic pole has implication on drifting subpulses and the observed drift rate. Drifting subpulses manifest as a systematic flow of subpulses across the pulse window resulting in tracks traced by the drifting subpulses in consecutive pulses. A parameter, known as P_2 , is used to describe the separation between two consecutive subpulses. In our model, P_2 corresponds to the time interval that the visible point takes to cut two consecutive emission spots. Another parameter, designated as P_3 , represents the time for the drift pattern to repeat once, with the drift rate given by P_2/P_3 . A distinction can be made between the flow of subpulses around the magnetic axis and the observed drifting of subpulses through the line of sight. The former corresponds to movement of the radial spokes in our model around the magnetic pole (along the $\psi = 0$ axis) towards either increasing or decreasing ϕ_b depending on the drift direction. This movement can be steady or varying being a function of ϕ_b . In either case, a relative motion exists between the visible point and the spokes, with the magnitude changes along the trajectory of the visible point. This relative motion contributes to the observed separation between the emission spots. We consider constant movement of spokes toward more positive ϕ_b and a viewing geometry represented by the trajectory of the visible point in solid green where ψ advances from

-180° to 180° as the pulsar rotates. The visible point will encounter emission spots moving in opposite direction between $|\psi| \gtrsim 40^\circ$ giving a higher relative motion. For $|\psi| < 40^\circ$, the emission spots appear to move in opposite (same) direction for slower (faster) moving spokes than the visible point with both situations leading to a slower relative motion. It is apparent from Fig. 2 that the difference in the measured separation between consecutive emission spots (P_2) and the flow rate of the radial spokes around the magnetic axis is dependent on ζ, α , with the difference intensifies for increasingly smaller $|\beta|$. Assuming P_3 is constant, the variations in P_2 imply changes in the drift rate. Therefore, measurement of drifting subpulses is inevitably linked to the emission geometry of the pulsar.

There are obvious limitations in our model. Firstly, we assume circular carousel layers, with uniform arrangement of emission spots on each layer, and concentric at the magnetic axis in a pure dipolar field structure. The resulting emission geometry is self-similar in the sense that the traversal of an emission spot by the trajectory of the visible point is independent of r . The observed asymmetric separation between the mainpulse and interpulse in PSR B0826–34 implies deviation of the above assumptions. A more accurate model will need to include the distortional effects due to the r^{-2} and r^{-1} terms in the magnetic field equation. In this case, a circular carousel layer is expected to become more distorted as it locates increasingly away from the magnetic axis and the associated distribution of emission spots is unlikely to be uniform anymore but will also be dependent on r and ϕ_b . Secondly, pulsar emission is attributed to highly relativistic particles propagating along magnetic field lines and directed along the velocity of the particles, which is not strictly along the magnetic field line but vastly confined to a narrow forward

cone. Furthermore, the cone angle is not zero and the angular difference between the axis of this cone and the field line is proportional to emission height. For a pure dipolar structure, as we assumed in this investigation, which applies only to the lowest order in an expansion in r/r_L , these deviations are small and can be included as perturbations. In its present form, our model is incapable of predicting the conical structure and offers no information on the grouping of the emission spots into either inner or outer cones within a profile.

Acknowledgements We thank the XAO pulsar group for discussions. We also thank the anonymous referee for useful comments which have improved the presentation of this paper.

References

- [1] Lyne A G, Manchester R N. MNRAS, 1988, 234: 477
- [2] Rankin J M. ApJ, 1990, 352: 247
- [3] Rankin J M. ApJS, 1993, 85: 145
- [4] Gupta Y, Gangadhara R T. ApJ, 2003, 584: 418
- [5] Dyks J. MNRAS, 2017, 471: L131
- [6] Kramer M, Wielebinski R, Jessner A, et al. A&AS, 1994, 107: 515
- [7] Krishnamohan S, Downs G S. ApJ, 1983, 265: 372
- [8] Wu X J, Gao X Y, Rankin J M, et al. AJ, 1998, 116: 1984
- [9] Gangadhara R T, Gupta Y. ApJ, 2001, 555: 31
- [10] Gil J A, Kijak J. A&A, 1993, 273: 563
- [11] Kramer M. A&AS, 1994, 107: 527
- [12] Rankin J M. ApJ, 1983, 274: 333
- [13] Rankin J M. ApJ, 1983, 274: 359
- [14] Rankin J M. ApJ, 1993, 405: 285
- [15] Deshpande A A, Rankin J M. ApJ, 1999, 524: 1008
- [16] Deshpande A A, Rankin J M. MNRAS, 2001, 322: 438
- [17] Edwards R T, Stappers B. A&A, 2002, 393: 733
- [18] Fan G L, Cheng K S, Manchester R N. ApJ, 2001, 557: 297
- [19] Gil J A, Sendyk M. ApJ, 2000, 541: 351
- [20] Rankin J M, Wright G A E. A&ARv, 2003, 12: 43
- [21] Ruderman M. ARA&A, 1972, 10: 427
- [22] Ruderman M A, Sutherland P G. ApJ, 1975, 196: 51
- [23] Clemens J C, Rosen R. ApJ, 2004, 609: 340
- [24] Gogoberidze G, Machabeli G Z, Melrose D B, et al. MNRAS, 2005, 360: 669

- [25] Fung P K, Khechinashvili D, Kuijpers J. A&A, 2006, 445: 779
- [26] Pétri J. A&A, 2007, 464: 135
- [27] Yuen R, Melrose D B. PASA, 2014, 31: e039
- [28] Cordes J M. ApJ, 1978, 222: 1006
- [29] Kijak J, Gil J. A&A, 2003, 397: 969
- [30] Hibsichman J A, Arons J. ApJ, 2001, 554: 624
- [31] Gangadhara R T. ApJ, 2004, 609: 335
- [32] Manchester R N, Taylor J H. Pulsars. Freeman: San Francisco, 1977: 13-20
- [33] Biggs J D, McCulloch P M, Hamilton P A, et al. MNRAS, 1985, 215: 281
- [34] Esamdin A, Lyne A G, Graham-Smith F, et al. MNRAS, 2005, 356: 59

Appendix

Transformation matrices

The transformation between the unit vectors $\hat{x}, \hat{y}, \hat{z}$ and $\hat{x}_b, \hat{y}_b, \hat{z}_b$ is given by

$$\begin{pmatrix} \hat{x}_b \\ \hat{y}_b \\ \hat{z}_b \end{pmatrix} = \mathbf{R} \begin{pmatrix} \hat{x} \\ \hat{y} \\ \hat{z} \end{pmatrix} \text{ and } \begin{pmatrix} \hat{x} \\ \hat{y} \\ \hat{z} \end{pmatrix} = \mathbf{R}^T \begin{pmatrix} \hat{x}_b \\ \hat{y}_b \\ \hat{z}_b \end{pmatrix}, \quad (5)$$

where

$$\mathbf{R} = \begin{pmatrix} \cos \alpha \cos \psi & \cos \alpha \sin \psi & -\sin \alpha \\ -\sin \psi & \cos \psi & 0 \\ \sin \alpha \cos \psi & \sin \alpha \sin \psi & \cos \alpha \end{pmatrix}, \quad (6)$$

and \mathbf{R}^T is the transpose of \mathbf{R} . For transformation between Cartesian to the respective unit vectors in spherical coordinates $\hat{r}, \hat{\theta}, \hat{\phi}$ and $\hat{r}_b, \hat{\theta}_b, \hat{\phi}_b$, we have

$$\begin{pmatrix} \hat{r} \\ \hat{\theta} \\ \hat{\phi} \end{pmatrix} = \begin{pmatrix} \sin \theta \cos \phi & \sin \theta \sin \phi & \cos \theta \\ \cos \theta \cos \phi & \cos \theta \sin \phi & -\sin \theta \\ -\sin \phi & \cos \phi & 0 \end{pmatrix} \begin{pmatrix} \hat{x} \\ \hat{y} \\ \hat{z} \end{pmatrix}, \quad (7)$$

and transforming vectors relative to the magnetic axis involve adding the subscript b to Equation (7).

脉冲星射电轮廓中高斯成分在主脉冲和中间脉冲的不同分布

韩晓红¹ YUEN Rai^{1,2,3}

(1 中国科学院新疆天文台 乌鲁木齐 830011)

(2 中国科学院射电天文重点实验室 南京 210023)

(3 悉尼大学物理学院 悉尼 NSW 2006)

摘要 研究了高斯辐射成分在可视点所画出轨迹上的分布, 这个可视点因脉冲星的转动而作非匀速度运动. 通过假设辐射区域围绕磁轴均匀分布, 一个高斯辐射成分便对应于可视轨迹划过的一个辐射区域. 因为演示辐射区域在可视轨迹上是不均匀的分布, 因此高斯成分沿轨迹也是不均匀的, 而高斯成分的密度在磁轴与视线距离最近时为最大. 高斯成分的分布取决于脉冲星的两个角度: 旋转轴和视线之间的夹角, 以及磁轴和旋转轴之间的倾角. 基于此模型, 一个脉冲星平均轮廓中观察到的多个高斯成分便对应于可视轨迹在特定的转动相位范围内的辐射区域. 演示了脉冲星旋转的近侧和远侧的相位, 分别对应的主脉冲和中间脉冲, 两者高斯成分的数量和分布是不同的. 而且还发现, 沿可视轨迹上的辐射区域总数与围绕磁轴的辐射区域的总数是不同, 并且预测的辐射区域数目会因忽略可见点的运动而明显不同. 拟合表明脉冲星轮廓的高斯成分的形状和数量可能与实际构成轮廓的成分的形状和数量不同. 以PSR B0826-34的辐射为例, 并假设辐射来自单一磁极.

关键词 辐射机制: 非热, 脉冲星: 普通, 方法: 分析